RESEARCH ARTICLE

Lithium-Ion Batteries

Energy & Environmental Materials WILEY

One-Step Synthesis of Si–Graphene Heterostructures via in-Flight Gas-Phase Mixing for High-Capacity Silicon-Rich Anodes

Muhammad Ali, Mukarram Ali, Yasaman Jarrahizadeh, Axel Lorke, Michael A. Pope, and Hartmut Wiggers**

The deliberate assembly of heterostructures has emerged as a powerful strategy for electrochemical energy storage, where integration of complementary components enables synergistic performance gains. Moving beyond serial production of individual components and their subsequent liquid-phase assembly, we report a one-step, continuous gas-phase synthesis of high-purity silicon/few-layer graphene heterostructures by coupling microwave-plasma and hot-wall reactors. This in-flight assembly yields exceptionally pure amorphous Si uniformly integrated within conductive few-layer graphene, eliminating liquid-phase processing. Electrochemical performance exhibits a non-monotonic dependence of performance on few-layer graphene content: capacity and cycle life maximize at an intermediate 15 wt.% few-layer graphene, attributed to a percolated, strain-buffering few-layer graphene network that preserves electrical contact while minimizing inactive mass. The optimized heterostructure delivers specific capacities of ∼2800 mAh g^{-1}_{Si+FLG} (0.05 C) and ∼1400 mAh g^{-1}_{Si+FLG} after 100 cycles at 1 C, outperforming other Si/graphene systems reported in the literature under similar conditions. These results highlight gas-phase self-assembly as a scalable route to integrate 0D/2D nanostructures into high-capacity, long-life Li-ion anodes and establish a new performance benchmark for low-carbon-fraction Si/graphene composites.

1. Introduction

Two-dimensional (2D) graphene emerged as a transformative material for electrochemical energy storage due to its high surface area, outstanding intrinsic electrical conductivity, mechanical robustness, and (electro)chemical stability.[1–3] These properties enable rapid electron transport, facilitate efficient ion diffusion, and provide structural integrity under electrochemical operation, making graphene an ideal platform for designing next-generation electrode architectures.[4] In particular, its integration with high-capacity active materials offers a compelling route to overcoming long-standing challenges in lithium-ion batteries.[5,6] Silicon (Si) exhibits a significantly higher theoretical capacity than graphite (3579 vs 372 mAh g^{-1}), making silicon-rich anodes a promising material for next-generation, higher energy density Li-ion batteries; however, the practical implementation of Si has been limited due to its poor electrical conductivity and severe volume fluctuations during lithiation and delithiation.[5,7–11] By acting as a functional conductive and mechanically resilient buffer, graphene can effectively enhance charge transport and mitigate structural degradation, thereby unlocking the practical potential of Si-based anodes for durable, high-performance lithium-ion batteries.[7,12]

Extensive research has focused on the synthesis and integration of graphene with silicon nanoparticles to address the challenges related to silicon-based anodes in Li-ion batteries.[13–15] Recently, work on the production of Si/carbon composites has focused on two main integration approaches: physical blending,[11,16–20] where presynthesized Si nanocrystals are mixed with graphene and other carbon (C) based materials, and chemical syntheses involving reaction-based techniques.[21–23] Within these broader categories, there are several different methods employed to combine and achieve novel architectures of Si and graphene and tune their electrochemical performance. These approaches span conventional solvothermal methods[24] to more advanced techniques of electrospinning, spray drying, and freeze drying.[25–28] In addition, innovative core–shell and yolk–shell architectures as well as composites involving functionalized Si and doped graphene are also achieved using novel production techniques.[29–34]

M. Ali, Prof., Dr. H. Wiggers
EMPI, Institute for Energy and Materials Processes – Reactive Fluids, University of Duisburg-Essen, Carl-Benz-Straße 199, Duisburg 47057, Germany
E-mail: m57ali@uwaterloo.ca
E-mail: hartmut.wiggers@uni-due.de
M. Ali, Dr. M. Ali, Dr. M. A. Pope
Department of Chemical Engineering, University of Waterloo, 200 University Avenue W, Waterloo N2L 3G1, Ontario, Canada
E-mail: michael.pope@uwaterloo.ca
Y. Jarrahizadeh, Prof. A. Lorke
Faculty of Physics, University of Duisburg-Essen, Lotharstraße 1, Duisburg 47057, Germany
Prof. A. Lorke, Prof., Dr. H. Wiggers
CENIDE, Center for Nanointegration Duisburg-Essen, University of Duisburg-Essen, Carl-Benz-Str. 199, Duisburg 47057, Germany
The ORCID identification number(s) for the author(s) of this article can be found under https://doi.org/10.1002/eem2.70333.

DOI: 10.1002/eem2.70333

Although graphene holds significant promise in addressing the limitations of Si, the simultaneous synthesis and integration of both components, while preserving their intrinsic structural and functional properties, remains a considerable challenge, particularly in achieving scalable production. The existing synthesis methods are often constrained by significant limitations such as limited scalability, requirements of high-temperature heat treatments, contamination during chemical processing, and challenges in processing high-purity graphene.[35,36]

Among emerging approaches, gas-phase synthesis is a promising strategy for highly efficient and scalable production of nanomaterials such as fumed alumina and silica, carbon black, and metallic and ceramic nanoparticles, enabling control over composition and morphology.[7,37–40] In particular, gas-phase-synthesized few-layer graphene (FLG) exhibits exceptional properties, including ultra-high purity and excellent electrical conductivity ($\sim$4000 S m^{-1}), making it promising for enhancing electrochemical performance.[7,37,41–43] Moreover, gas-phase synthesis enables control over nanoparticle structure, particularly for Si, where forming amorphous particles is crucial as amorphous Si nanoparticles (nSi) can improve electrochemical performance by minimizing volumetric expansion stress and fracture propagation.[44] Intimate mixing on the nanometer scale of the respective nanopowders is usually only possible through surface functionalization and stabilization – usually in the liquid phase, which requires the addition of further chemical components, which in turn reduce the gravimetric capacity. Thus, preserving the material properties through conventional multistep synthesis involving intensive chemical processing and thermal treatment remains a significant challenge. Therefore, it is advantageous to explore and develop strategies that mitigate these effects to further exploit the functional potential of graphene in advanced energy applications.

Here, we present a one-step all gas-phase approach for the simultaneous synthesis and integration of silicon nanoparticles and FLG into Si–FLG heterostructures. Building on our previous work regarding gas-phase synthesis of the individual components,[7] the principal objective is to develop a continuous method for heterostructure formation that preserves the distinct structural and functional properties of each constituent, whereby additional stabilization or functionalization is avoided. This is accomplished by the development of a coupled reactor system comprising a microwave (MW) plasma reactor and a hot wall reactor, enabling a co-gas phase synthesis of nSi–FLG heterostructures. The synthesized heterostructures are characterized by their structural and morphological features, as well as subjected to exploration of electrical transport properties and electrochemical performance.

2. Results and Discussion

To validate the effectiveness and efficiency of the integration approach, a comprehensive analysis of the structural, morphological, and functional properties of the Si-FLG heterostructures was carried out.

2.1. Structural and Morphological Characterization

Powder X-ray diffraction (XRD) was performed to study the structural characteristics of Si-FLG heterostructures, as shown in **Figure 1a**. XRD profiles of all the heterostructures confirm nanocrystalline diamond-cubic Si as the only crystalline phase, with reflection peaks at $2\theta \approx 30°$, 47°, and 57° indexed to (111), (220), and (311) crystal planes for Si, respectively.[45] The FLG showed a peak at $2\theta \approx 26°$ corresponding to the (002) plane of graphite (consistent with few-layer). At low FLG loadings, this band is largely buried under the intense Si(111) peak, both because C scatters weakly, there is little FLG stacking order, and the mass fraction is Si-rich, so XRD underreports the graphene component.[7] However, the appearance of the FLG peak, despite its low concentration, indicates that the few-layer flakes exhibit a high degree of crystallinity. The S150 sample, synthesized at the lowest Si precursor flow rate, exhibits broadened Si reflections in the XRD pattern, consistent with nanocrystalline Si. In addition, the relatively stronger FLG (002) reflection indicates a higher FLG weight fraction compared to the other samples. On the other hand, samples synthesized with higher flow rates of Si precursor showed a progressive suppression of both the FLG and Si peaks in their diffraction patterns. We attribute this trend to kinetics and contrast effects rather than the emergence of new phases: i) higher precursor supersaturation accelerates nucleation, yielding a larger number of smaller Si domains (Scherrer broadening) and a higher amorphous Si fraction. ii) The decomposition of SiH_4 into Si and H_2 causes an increase in volume in the hot wall reactor, which leads to shorter residence time in the hot zone and limiting crystallite growth. iii) This shifts the chemical equilibrium of the reaction $SiH_4 = Si + 2H_2$ in the direction of the educt. Taken together, this leads to less crystallization of Si and correspondingly to a higher fraction of the desired amorphous silicon phase. On the other hand, it will lead to an incomplete SiH_4 decomposition and thus lower yield.

Following the XRD analysis, the mass fractions of Si and FLG, along with further insights into the structural characteristics of the synthesized Si-FLG heterostructures, were determined through parallel thermogravimetric analysis (TGA) and differential scanning calorimetry (DSC) measurements. The measurements were conducted from room temperature to 900 °C under air at a heating rate of 10 K min^{-1}. Figure 1b presents the TGA curves of all the synthesized Si–FLG heterostructures. The results show that, as the temperature exceeds 650 °C, FLG undergoes oxidative decomposition, releasing gaseous byproducts such as carbon dioxide (CO_2) and carbon monoxide (CO), resulting in significant mass loss.[46,47] FLG content was obtained from the baseline-corrected TG mass loss associated with C combustion in air; the endpoint was defined at the temperature where the DTG signal returned to baseline (complete FLG oxidation), prior to the onset of Si oxidation. Since Si starts reacting with oxygen (O_2) at temperatures above 800 °C, the formation of silicon dioxide (SiO_2) is the cause for the observed mass gain above this temperature.[48] The onset of mass loss at 650–700 °C, together with the steep TGA slopes, is characteristic of FLG oxidation rather than disordered or functionalized carbon species. The absence of additional low-temperature mass-loss steps further indicates negligible surface functionalization of the carbon component.[46] We have already demonstrated this in our earlier work using XPS analysis, in which we found that freshly produced FLG contains <1% oxygen and consists of more than 85% sp2 carbon.[7]

The weight percentage of FLG dropped from 31% to 4% when the Si precursor flow rate increased from 150 to 450 mL min^{-1}, according to TGA analysis. However, the content of FLG unexpectedly increased to about $\sim$6% when the precursor flow rate was 600 mL min^{-1}. The TGA results were also complemented by elemental analysis for C (see Figure S1, Supporting Information). As explained above, the increase in

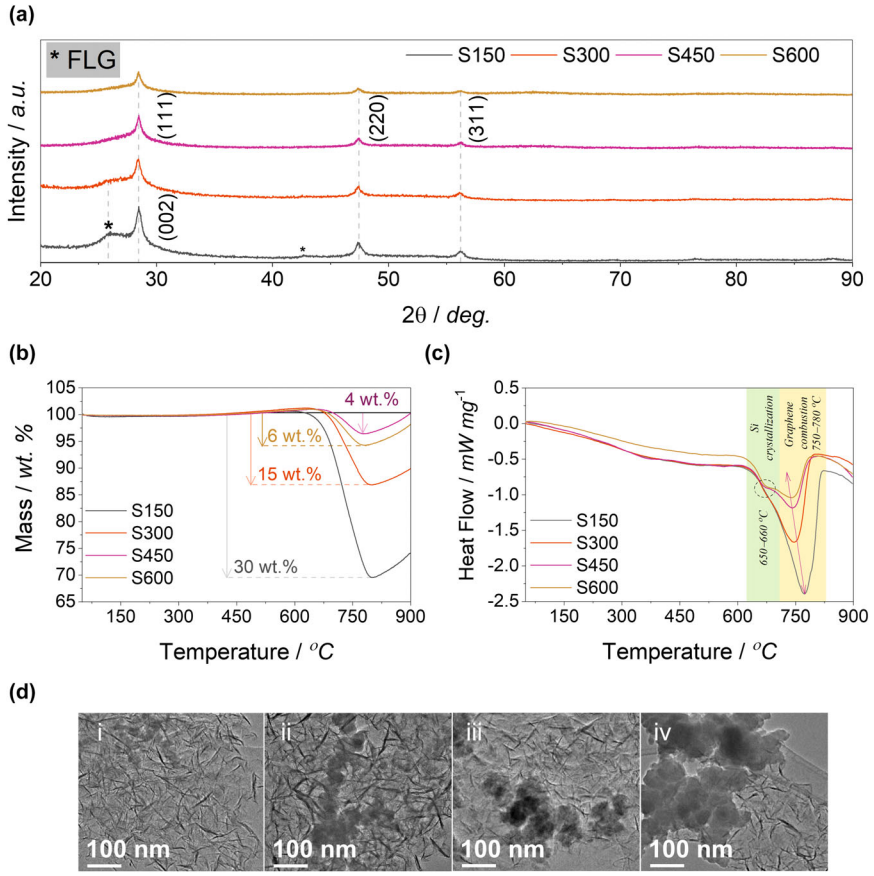

Figure 1. Structural, thermal, and morphological characterization of silicon/few-layer graphene (Si–FLG) heterostructures synthesized at different SiH_4 flow rates. a) X-ray diffraction (XRD) patterns showing characteristic peaks for silicon, whereas the graphene (002) peak is observable only for S150 and S300 at 26°. b) Thermogravimetric analysis (TGA) and c) differential scanning calorimetry (DSC) performed under air at 10 K min^{-1}, illustrating changes in mass fraction, oxidation behavior, and crystallization characteristics as a function of Si precursor flow rate. d) Transmission electron microscopy (TEM) images of Si-FLG heterostructures for different samples prepared at different SiH_4 flow rates: i) S150, ii) S300, iii) S450, and iv) S600.

FLG content for the S600 sample can be attributed to the incomplete pyrolysis of SiH_4 at the highest flow rate, which affects the composition of the resulting material and decreases the yield of Si.[40]

Figure 1c shows the results from DSC measurements exhibiting a major exothermic event corresponding to the oxidation of C at ~700 °C, which is also in accordance with the mass loss in TGA results.[47] Moreover, for heterostructures prepared at higher Si precursor flow rates (S450 and S600), in addition to the primary exotherm FLG oxidation, the DSC thermograms show a secondary exothermic shoulder. This peak can be attributed to the crystallization of amorphous Si, as it is a typical behavior for amorphous Si, which undergoes crystallization at temperatures above 650 °C before oxidation when heated in the presence of O_2.[49,50] The increased prominence of the crystallization exotherm at higher SiH_4 flow rates indicates a higher fraction of amorphous Si relative to samples synthesized at lower flow rates, while the combined TGA and DSC results identify an intermediate precursor flow rate that maximizes the yield of highly amorphous Si nanoparticles. Excessively high flow rates reduce Si yield, whereas lower flow rates favor increased crystallinity. Given the superior electrochemical stability of amorphous Si due to isotropic lithiation and improved accommodation of large volume changes, the balance between amorphous content and yield is critical.

In addition to structural and thermal analysis, morphological properties of the Si-FLG heterostructures were studied using transmission electron microscopy (TEM). Figure 1d shows the TEM images of Si-FLG heterostructures produced at varying Si precursor flow rates. A clear trend for nSi is observed wherein both particle size and the degree of agglomeration increase with higher precursor flow rates (see Figure 1d-i–iv). At the highest precursor flow (600 mL min^{-1}/S600), the elevated SiH_4 partial pressure produces a dense Si aerosol, so the n^2 dependence of Brownian coagulation and hot-zone sintering drives pronounced nucleation and nanoparticle aggregation.[51,52] Consequently, Si preferentially aggregates rather than uniformly decorating FLG surfaces, reducing the effective Si–FLG interfacial area and disrupting the percolated conductive network within the heterostructure. The higher degree of amorphousness and increased particle agglomeration at high Si precursor flow rate adversely affect the efficiency of mixing with FLG. These observations highlight the critical influence of synthesis parameters on the resulting morphology and interfacial integration of the components, underscoring the importance of precise control over synthesis conditions to ensure efficient heterostructure formation.

Furthermore, S300 was examined in detail to gain deeper insight into the Si-FLG interface. **Figure 2** shows the TEM images of S300 at different resolutions (see Figure 2a,b) and the corresponding high-resolution EDS mapping (see Figure 2c). The higher resolution TEM image revealed the coverage of nSi with FLG, whereas the lower resolution image illustrates the overall morphology of the heterostructures. The nSi particles exhibited a certain degree of aggregation and are surrounded by 2D FLG sheets. The crumpled character and small lateral dimensions of the FLG synthesized by gas-phase synthesis agree with previous studies.[43,53] Due to the relatively small size of the FLG flakes and the partial aggregation of nSi, complete coverage of the nanoparticles by FLG is not observed. However, the FLG sheets are clearly seen in close contact with the nSi, occupying the interparticle regions, and forming an interconnected network, as can be seen in the marked areas in Figure 2c. This intimate contact is indicative of effective physical integration between the two components within the heterostructure, which was achieved through hetero-aggregate formation in the gas phase. Furthermore, EDS confirms the presence of only nSi and FLG in the heterostructures, with no detectable impurity elements, which will be discussed in detail in Section 2.2. These results emphasize the effectiveness of the gas-phase

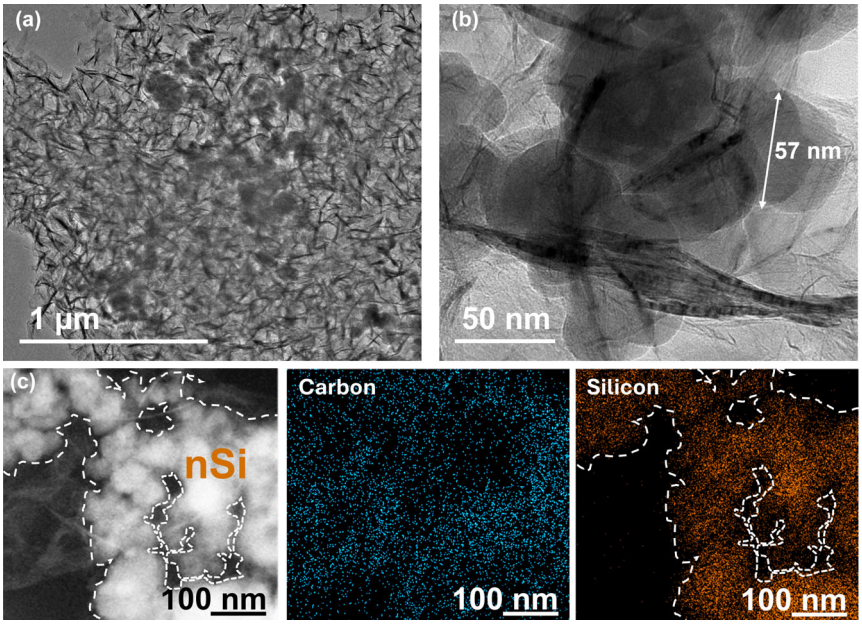

Figure 2. Morphological characterization of S300 by transmission electron microscopy (TEM). a) Low magnification image of S300 illustrating the homogeneous intermixing of amorphous silicon nanoparticles (nSi) with few-layer graphene (FLG). b) High magnification TEM images of S300 showing revealing nSi particles anchored within and bridged by a continuous few-layer graphene (FLG) scaffold. c) Energy-dispersive X-ray spectroscopy (EDS) elemental mapping confirming spatial co-localization of Si and C.

synthesis process and the excellent purity of the synthesized heterostructures.

2.2. Functional Characterization

Raman spectroscopy is a powerful tool for obtaining structural insights into materials and is particularly crucial for assessing and confirming the quality of graphene. The Raman spectra of nSi and FLG are shown in **Figure 3**a. The Raman spectrum of silicon typically exhibits features in the 400–550 cm^{-1} range, where the peak shape and position distinguish amorphous Si (broad band) from crystalline Si (sharp feature near 520–550 cm^{-1}).[54] In the present nSi sample, the inset highlighting the 400–500 cm^{-1} region (Figure 3a–i) shows a dominant broad amorphous-Si contribution with a weaker crystalline component, in agreement with the structural trends observed by XRD and DSC. The Raman peak for graphene at 1500 cm^{-1} corresponds to the symmetry-allowed E g mode at the Γ-point, commonly known as the G band, which arises from in-plane optical vibrations due to opposite movements of adjacent C atoms, leading to significant bond distortion.[55] The second peak at 2600 cm^{-1} corresponds to the 2D band, which originates from second-order Raman scattering involving transverse optical (TO) phonons near the K-point. Additionally, the weak D band observed around ∼1342 cm^{-1} can be attributed to TO phonons near the K-point, indicating minimal structural defects in the as-synthesized pristine FLG nanosheets.[55–57] The Raman spectra of FLG underscore the efficiency of the gas phase synthesis technique, which yields high-quality FLG with minimal defects, as evidenced by the stronger G band compared to the D band. Furthermore, the pronounced 2D band indicates minimal layer stacking, suggesting that FLG is dominantly composed of approximately 3 to 6 layers.

Figure 3b shows the Raman spectra for the synthesized Si-FLG heterostructures. The distinctive peaks that pure nSi and FLG, respectively, displayed in Figure 3a were used as a benchmark for the composite composition. As the weight percentage of nSi in the composite increases from S150 to S600, a noticeable pattern becomes apparent. It was observed that the intensity of the FLG peaks gradually decreased from S150 to S600, indicating a change in the nSi to FLG ratio. Nevertheless, no peak shift for FLG is observed for Si-FLG heterostructures in the Raman spectra, which indicates preservation of structural and functional properties of the FLG. Furthermore, the I_D/I_G ratio, defect density (n_D), and inter-defect distance (L_D) of FLG were calculated using the following equations:[58]

$$L_D = (1.8 \pm 0.5) \times 10^{-9} \lambda_L^4 \left(\frac{I_D}{I_G}\right)^{-1} \quad (1)$$

$$n_D = \frac{(1.8 \pm 0.5) \times 10^{22}}{\lambda_L^4} \left(\frac{I_D}{I_G}\right) \quad (2)$$

where λ_L denotes the excitation wavelength used for Raman measurements (633 nm). Figure 3c summarizes the values obtained for I_D/I_G and n_D. Relative to pristine FLG, Si–FLG powders show a modest increase in I_D/I_G and n_D as the FLG fraction decreases, consistent with a small increase in edge/anchoring sites, where nSi pin or slightly fragment the flakes during aerosol mixing. The values remain within the stage-1 disorder regime, indicating that the sp^2 network is largely preserved. Additionally, G and 2D band positions are unchanged within experimental uncertainty, with no systematic broadening, which argues against measurable strain or doping induced by the heterostructure process and is consistent with maintained electronic pathways in the FLG scaffold.[59] Across all the samples, I_{2D}/I_G remained stable (>1) and shows a slight increase for the Si-FLG heterostructures; this behavior is consistent with reduced restacking/partial decoupling of FLG layers as nSi nanoparticles space the flakes (see Table S1, Supporting Information). Taken together, the Raman data indicate that nSi loading slightly increases defect/edge density but does not compromise few-layer character or sp^2 continuity, which is favorable for charge transport in the composite anodes.

The electrical conductivity of the Si-FLG heterostructures was measured using the four-point probe method. Figure 3d shows the bulk conductivity and specific surface area (SSA) versus FLG content, revealing a percolation-controlled response. While the four-point probe technique provides high accuracy for compact, homogeneous, and well-contacted samples, limitations arise in the case of powder-based and porous nanomaterials.[60–62] In nano-powders and nanocomposites with varying morphologies, factors such as anisotropy, porosity, and inhomogeneity typically influence overall charge transport.[63,64]

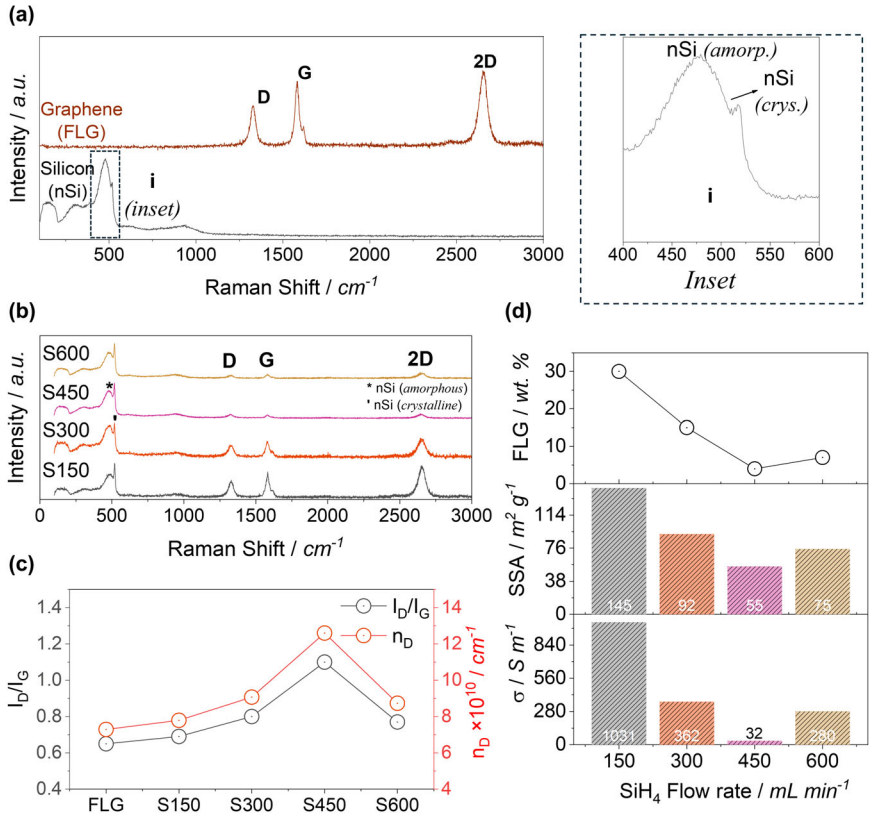

Figure 3. Structural and transport properties of nSi, few-layer graphene (FLG), and Si–FLG heterostructures. a) Raman spectra of pristine nSi and FLG. b) Raman spectra of Si–FLG heterostructures showing progressive suppression of graphene features with increasing Si precursor flow rate. c) Extracted I_D/I_G ratios and defect density (nD) values for Si–FLG heterostructures. d) Electrical conductivity and Brunauer–Emmett–Teller (BET) specific surface area as a function of FLG content.

Accordingly, conductivity analysis accounted for sample preparation, porosity, and composition in addition to the intrinsic conductivities of pristine nSi and FLG. To minimize variability, all samples were prepared under identical conditions by uniaxial pressing at 650 MPa for 5 min. Bulk density and porosity were calculated to verify preparation consistency (Figure S2, Supporting Information), revealing moderate compaction with porosity values in the narrow range of 45–50% across all compositions. The sample S150 showed the highest electronic conductivity of 1031 $S\,m^{-1}$, as it contains the highest FLG loading (30 wt.%). As the structural analysis in Section 3.1 indicated the dominant amorphous nature of nSi, which typically shows very low conductivity on the order of $\sim 10^{-5}\,S\,m^{-1}$,[65] the high electrical conductivity ($\sim 4000\,S\,m^{-1}$)[7] of FLG played the important role in enhancing the overall conductivity of the Si–FLG heterostructures. The variation in conductivities of different samples clearly corresponds to the varying concentration of FLG. The percolation threshold for conductivity was determined by fitting a percolation power law to the experimental data (see Figure S3, Supporting Information). The threshold was found to be 2.9 vol.% (corresponding to ~2.8 wt.%) for FLG, which is very close to values reported in literature for similar anisotropic 2D systems.[66] This confirms that the conductive pathways formed by FLG are crucial for enhancing electron transport in the almost insulating Si matrix, a key limiting factor for anode applications in Li-ion batteries. In addition to the conductivity, the SSA is another critical parameter for electrochemical performance, as it facilitates charge transfer and stable solid–electrolyte interface (SEI) formation. Figure 3d-ii presents the SSA of the Si–FLG heterostructures determined by the Brunauer–Emmett–Teller (BET) method. The SSA trend closely follows the variation in FLG content: in samples S150, S300, and S450, decreasing FLG content led to reduced SSA, while the higher FLG content in S600 increased it. Owing to its high surface area ($\sim 320\,m^2\,g^{-1}$) compared to Si ($\sim 30\,m^2\,g^{-1}$), FLG synthesized via MW plasma strongly contributes to the overall SSA.[7] The maximum SSA was observed to be 145 $m^2\,g^{-1}$ for S150 (30 wt% FLG). Moreover, even at 5 wt.% FLG (S450), the SSA nearly doubled relative to pure Si, underscoring the pronounced influence of FLG on the surface properties of heterostructures.

2.3. Electrochemical Characterization and Performance

For electrochemical evaluation, slurry-cast Si-FLG electrodes are prepared on Cu current collectors as detailed in the Section 4. The scanning electron microscopy (SEM) images of the Si-FLG cast into electrodes (see Figure S4b, Supporting Information) show that FLG appears as web-like sheets that partially wrap and bridge the nanoparticles. This interleaving is expected to suppress secondary Si-Si agglomeration and establish a percolated carbon pathway, lowering contact resistance and improving mechanical integrity.

Figure 4a,b present the galvanostatic charge discharge (GCD) and dQ/dV profiles, respectively, for pristine nSi and the Si-FLG heterostructures. Figure 4a shows the formation cycle at 0.05 C. All electrodes display the expected sharp drop from ~1.2 V on first lithiation, reflecting electrolyte reduction and SEI formation. This is then followed by a featureless, sloping lithiation down to 0.01 V with no discernible two-phase plateau. This behavior is characteristic of amorphous Si with broad a-Li_xSi formation.[44,67,68] Pristine nSi demonstrated a high initial discharge capacity of 3507 ± 50 mAh g^{-1} (due to its higher active Si content) as compared to 3134 ± 50, 2808 ± 50, and 2252 ± 50 mAh g^{-1} for S450, S300, and S150 Si–FLG samples, respectively. Pristine Si and S450 exhibited slightly higher initial coulombic efficiency (ICE) of ~86% due to their lower SSA (55 $m^2\,g^{-1}$), compared to 81% for S300 (92 $m^2\,g^{-1}$), while S150 (145 $m^2\,g^{-1}$) showed a further decrease to 73%. This trend correlates directly with the SSAs determined by BET analysis, indicating that the higher electrolyte accessible surface area promoted by higher FLG content causes greater electrolyte decomposition and SEI formation during the first cycle, thereby consuming more Li irreversibly. Moreover, relative to pristine nSi, the Si-FLG composites (especially S300) exhibit a smaller charge–discharge gap at a given capacity (lower polarization) and a larger reversible portion of the first cycle, consistent with better electronic percolation and mechanical buffering by FLG; S150 shows lower gravimetric capacity due to its higher FLG fraction.

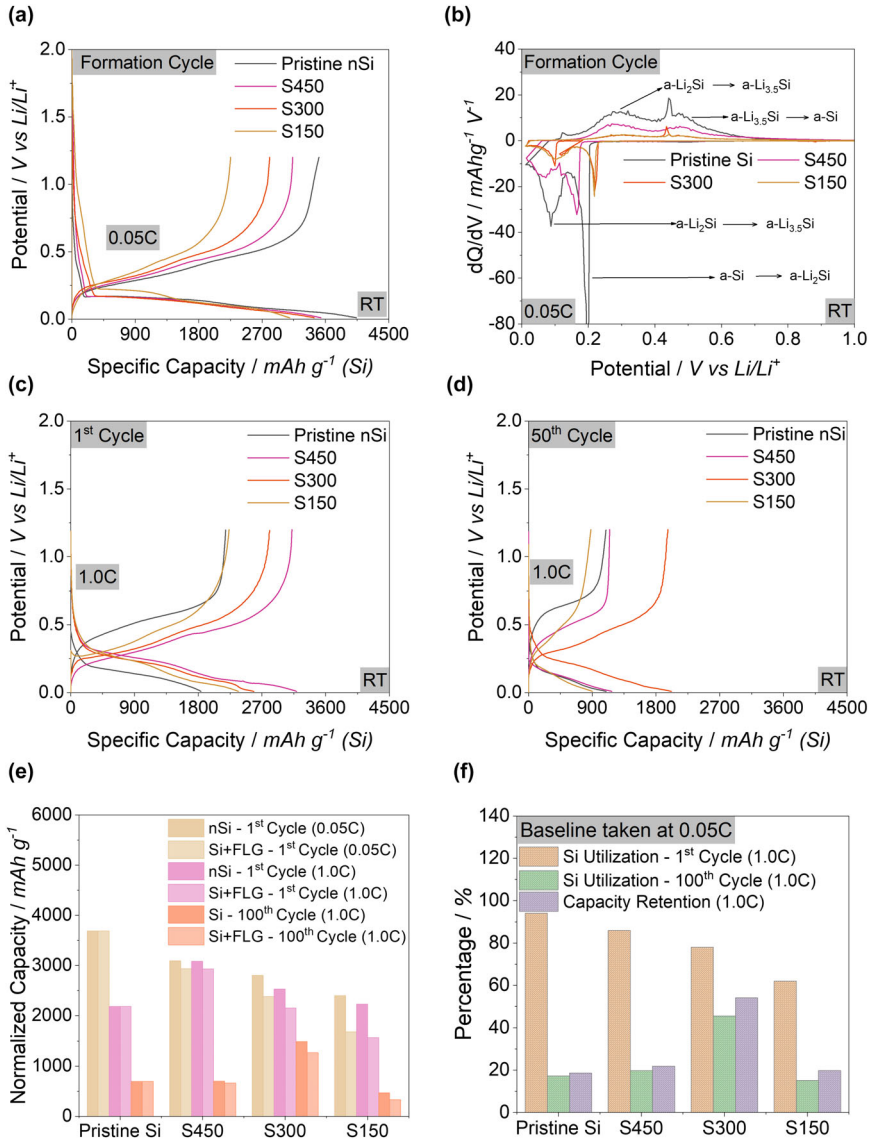

Figure 4. Electrochemical analyses of pristine nSi and Si/few-layer graphene (Si-FLG) heterostructures by galvanostatic charge discharge (GCD) profiles and differential capacity (dQ/dV) analysis. a) GCD profiles of the formation cycle (0.05 C). b) Corresponding formation-cycle dQ/dV curves highlighting the lithiation/delithiation features and phase evolution of Si. c) GCD profiles of the 1st cycle at 1C, and d) the 50th cycle at 1C. e) Comparison of discharge capacity normalized as per Si mass and total active (Si + FLG) mass for the formation, 1st and 100th cycle. f) Si utilization during formation, 1st and 100th cycle, and capacity retention at 100th cycle.

Figure 4b presents the differential capacity (dQ/dV) profiles (corresponding to the formation cycle) of pristine nSi and Si-FLG heterostructures, highlighting the characteristic two-step alloying/dealloying of amorphous nSi with Li. Pristine nSi exhibits a pronounced cathodic lithiation spike at a low potential of ~0.2 V, followed by a shoulder at ~0.08 V, consistent with the stepwise transformation of amorphous nSi into $Li_{3.5}Si$.[69,70] On delithiation, two distinct anodic peaks at 0.30–0.35 V and 0.45–0.55 V confirm the reversible extraction of Li and the re-formation of amorphous nSi. The dQ/dV profiles of Si-FLG heterostructures highlight the impact of FLG on the lithiation/delithiation process, especially S150 and S300, the lithiation and delithiation peaks are broader and less intense, indicating that FLG effectively moderates the abrupt phase transitions that are otherwise associated with severe volumetric strain of Si. Additionally, the heterostructures also displayed reduced peak hysteresis, reflecting diminished polarization and improved charge-transfer kinetics. At 1C, in pristine Si, the two-step alloying features progressively faded to one significant feature, and the hysteresis between lithiation and delithiation peaks widened, signaling the progressive loss of electrochemically active Si, contact loss, and severe structural degradation. Interestingly, at 1C, the Si-FLG heterostructures, particularly S150 and S300, retain their two-step alloying/dealloying characteristics even after extended cycling, without any appreciable increase in hysteresis (see Figure S5, Supporting Information). demonstrating effective mechanical and electronic stabilization by the FLG network. After the formation cycle, all samples display the expected rate-induced overpotential at 1C, with lithiation curves shifting to lower voltages and delithiation curves to higher voltages relative to 0.05C (see Figure 4c,d). Absolute capacities at 1 C (1st cycle) are 1839, 3187, 2584, and 2365 mAh g^{-1} for pristine nSi, S450, S300, and S150, respectively, as can be observed in Figure 4c. This corresponds to utilizations of ~45.5%, 89.8%, 75.4%, and 76.4% of their 0.05 C values. Among the composites, S300 exhibits the lowest polarization and the largest reversible capacity fraction, consistent with a percolated FLG network that homogenizes lithiation and lowers electronic and junction resistances. With continued cycling at 1C, pristine nSi and S450 develop pronounced polarization and capacity contraction, whereas S300 preserves both capacity and curve shape with only modest hysteresis increase. S150 shows faster fading due to lower active-Si content and enhanced surface-area-driven SEI growth. These trends are consistent with the dQ/dV evolution, where S300 maintains stable amorphous-Si features while pristine nSi collapses to a single broadened response.

Figure 4e,f consolidate the first cycle and rate-retention metrics. In Figure 4e, the ordering of first-discharge capacities (pristine nSi > S450 > S300 > S150) reflects the decreasing active-Si mass fraction in the composites, whereas the ICE exhibits an inverse correlation with BET SSA, consistent with greater electrolyte-accessible area promoting parasitic reactions/SEI growth at higher FLG contents. Figure 4f shows active-material utilization, defined as the specific capacity under the stated condition normalized to each material's 0.05 C formation capacity. The normalized utilizations at 1 C (1st cycle) are 92.5%, 89.8%, 84.0%, and 76.4% for pristine nSi, S450, S300, and S150, respectively; after 100 cycles at 1C they decline to 17.2%, 19.7%, 45.5%, and 15.1%. Notably, S300 sustains ~3× higher

utilization than pristine nSi at 1C after 100 cycles and the highest capacity retention, indicating that an intermediate FLG loading optimizes the trade-off between active-Si content and a percolated strain-buffering carbon network with lower charge-transfer/transport impedance, thereby supporting long-term rate performance.

Electrochemical impedance spectroscopy (EIS) plots of pristine Si-FLG heterostructures are shown in **Figure 5** and Figure S6, Supporting Information. The values of resistances (ohmic resistance R_s, SEI resistance R_{SEI}, interphase resistance R_{int}, and charge transfer resistance R_{ct}, see Supporting Information) are obtained by fitting an equivalent electrical circuit and are summarized in Table S2, Supporting Information. Pre-cycled electrodes measured at OCV (~1.2 V vs Li/Li^+) exhibit a clear trend (Figure 5a): pristine Si shows a large high-/mid-frequency semicircle, whereas S300 displays a markedly smaller one. At this stage, a stable SEI has not yet formed, so that R_{SEI} can be omitted from the circuit, and only interphase resistance R_{int} and charge transfer resistance R_{ct} are considered. The R_s is similar for most electrodes (≈8.5–9.6 Ω), except S150 (15.78 Ω). The R_{ct} value for S300 was found to be the lowest among all the compositions (nSi: 91 Ω < S450: 38 Ω < S300: 11 Ω < S150: 35 Ω), demonstrating that the gas-phase–formed FLG network provides efficient electronic pathways even before cycling. At low frequencies, pristine Si presents a relatively low Warburg slope, indicating increased kinetic limitations, while S300 exhibits steeper, more vertical tails, indicative of less restricted diffusion and enhanced capacitive behavior.

Figure 5b,c, and Figure S6, Supporting Information show Nyquist plots at 0.01 V (after lithiation) at selected cycles (formation, 50th, and 100th) for pristine nSi and Si–FLG heterostructures, respectively. Nyquist plots of nSi show a significant enlargement of the high-frequency semicircle from the formation cycle to the 50th cycle, then shrinking after 100 cycles. This trend is also reflected in fitted resistances (R_{SEI}, R_{ct}), which increase from the formation to the 100th cycle (R_{SEI}: 4.7 Ω → 7.5 Ω → 13 Ω, R_{ct}: 4.5 Ω → 12 Ω → 39 Ω), indicating continuous SEI growth and progressive loss of particle–particle contact. The low-frequency Warburg tail became more flattened with cycling, reflecting increasingly hindered Li^+ diffusion due to Si pulverization and SEI thickening. In contrast to pristine nSi, the S300 shows a markedly different evolution. A relatively large high-frequency semicircle is observed after the formation cycle, accompanied by a high R_{int} (~91 Ω), signifying that the interphase is not yet fully conditioned. By the 50th cycle, this semicircle shrinks, and R_{int} decreases sharply to ~42 Ω, after which it remains essentially stable through the 100th cycle (~43.6 Ω). S300 also undergoes only modest variation in R_{ct} (25 Ω → 26 Ω → 20 Ω), indicating stable charge-transfer kinetics. R_{SEI}, although it increases from 4.2 Ω to 7.5 Ω between the formation and 50th cycles, it plateaus thereafter (~8.4 Ω), demonstrating early SEI growth followed by stabilization rather than continuous thickening. The low-frequency response exhibits a steeper, more capacitive Warburg tail than pristine Si, consistent with less restricted Li^+ diffusion and preserved electronic percolation. These features indicate that the FLG scaffold stabilizes the SEI and maintains interparticle contact,

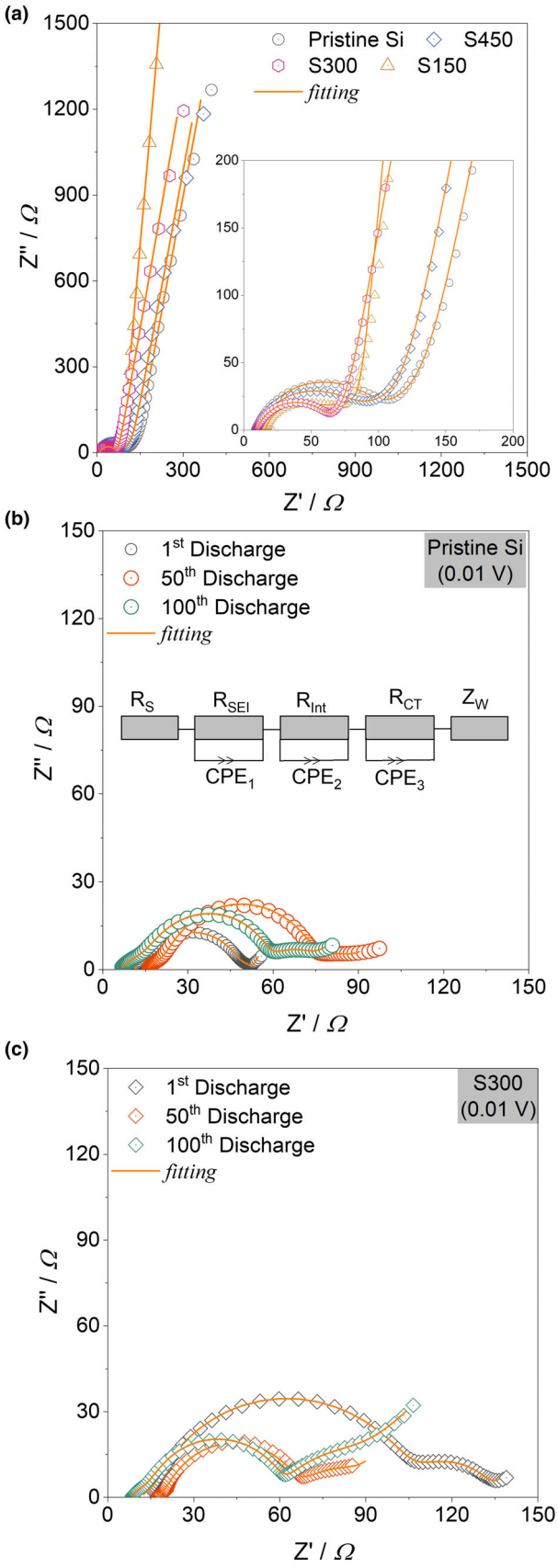

Figure 5. Electrochemical impedance spectroscopy (EIS) analysis of pristine nSi and Si/few-layer graphene (Si–FLG) heterostructures. a) Nyquist plots measured at open-circuit voltage (OCV) prior to lithiation. b) Evolution of impedance spectra for pristine nSi after the first, 50th, and 100th discharge at 0.01 V. c) Corresponding impedance spectra for S300 measured under identical conditions.

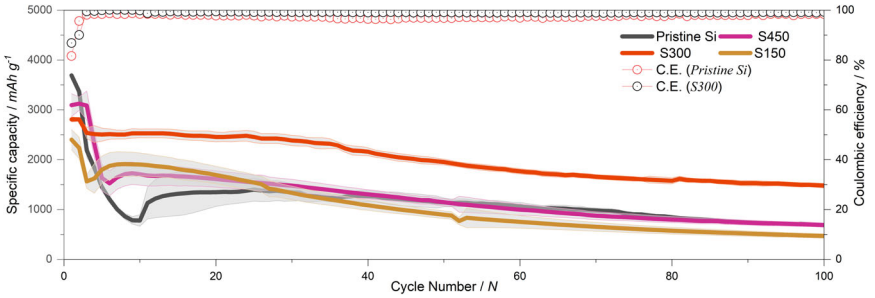

Figure 6. Cycling stability of nSi and Si/few-layer graphene (Si-FLG) heterostructures for 100 cycles with corresponding Coulombic efficiencies. The shaded region shows the standard deviation between the performance of three cells tested for each sample.

effectively suppressing the kinetic and transport degradation observed in pristine Si. EIS plots of S450 and S150 followed a similar trend as S300, but neither composition achieves the simultaneous conditions observed in S300: a percolated yet not overly dense FLG scaffold, moderate surface area (see Figure 3d), and stabilized R_{int}/R_{ct} evolution (see Table S2, Supporting Information). Overall, the impedance evolution demonstrates that long-term cycling stability in S300 arises from the preservation of stabilized charge transfer kinetics and SEI, enabled by a continuous, strain-buffering FLG network that prevents contact loss and diffusion bottlenecks.

The cycling stability, as shown in **Figure 6**, further highlights the enhanced performance of the Si-FLG heterostructures compared to pristine Si. The cycling is performed at a high current of 1C. S300 shows significantly stable cycling profiles compared to those of other samples, including pristine nSi. After 100 cycles, the Si-FLG heterostructures (S300) retained a discharge capacity of around 1480 mAh g^{-1} compared to 600 mAh g^{-1} of pristine nSi. An ICE of >80% is observed for both pristine Si and Si-FLG heterostructures (S300). The samples S450 and S150 suppress the large early-cycle drop observed in pristine nSi but trail S300 at a higher number of cycles. These results indicate that 15 wt. % FLG loading maximizes long-term utilization by balancing active-Si content with an effective conductive scaffold. A slurry-mixed Si + FLG (control) sample was prepared with FLG loading to evaluate the efficiency of gas-phase integration relative to physical or wet-chemical mixing. The electrochemical testing reveals lower capacities at 1C and faster capacity fading (Figure S7, Supporting Information), confirming that physical mixing alone cannot reproduce the percolated, strain-tolerant architecture achieved through gas-phase integration. The post-mortem SEM images provide key insights into the structural integrity of the nSi and S300 anodes after cycling (see Figure S8, Supporting Information). While pristine nSi anode underwent significant morphological destruction, including severe cracking of the electrode and pulverization of Si particles, the S300 anode maintained much of its original morphology. The FLG scaffold effectively mitigated the mechanical stresses induced by Si's volumetric changes during cycling, preventing excessive cracking and fragmentation. This preserved electrode integrity is crucial for maintaining electrochemical performance over long-term cycling. The continuous, percolated FLG network appears to act as a strain-buffering layer, accommodating Si's volume expansion and contraction without compromising the structural stability of the electrode. These findings highlight the superior performance of gas-phase integrated Si/FLG heterostructure composites in maintaining both the mechanical integrity and electrochemical functionality of Si-based anodes.

Compared to previously reported Si/graphene anodes, achieving stable cycling with only 15 wt% FLG represents a substantial reduction in carbon content relative to typical wet-chemical Si/graphene composites, which often require 30–40 wt% carbon to attain comparable cycling stability (Table S3, Supporting Information). In many of these systems, improved stability is obtained through multi-step processing, graphene oxide (GO) reduction, or chemical functionalization, which increases synthesis complexity and introduces additional interfacial chemistry. By contrast, the present gas-phase approach delivers an initial discharge capacity of ~2800 mAh g^{-1} with an ICE of 86%, placing it among the highest-performing Si/graphene systems reported under comparable conditions (Table S3, Supporting Information), while relying on a significantly lower carbon fraction. Collectively, these results highlight the unique advantages of gas-phase synthesis, where the exceptionally low percolation threshold and high-purity FLG network synergistically yield superior electrochemical stability, high reversibility, and minimal irreversible loss during initial cycling.

Gas-phase self-assembled Si-FLG heterostructures outperformed wet-chemically integrated composites in several key metrics, particularly in terms of scalability, capacity, and ICE, where a similar quality of gas-phase synthesized FLG was used.[7] Previously reported initial discharge capacity for Si/gas-phase graphene (GPG) composites was 2200 mAh g^{-1} with good long-term stability at 0.5 C. In contrast, Si-FLG heterostructures achieve an initial discharge capacity of ~2808 mAh g^{-1} and retain ~1480 mAh g^{-1} after 100 cycles at 1 C with much lower carbon content (15 wt.% vs. 24 wt.% FLG). Notably, we achieved 86% ICE (compared to 77%), which is indicative of reduced irreversible losses.

Our results also demonstrate that gas-phase synthesis enables a high-quality, percolated FLG network around Si nanoparticles, significantly lowering the percolation threshold and improving long-term stability. The gas-phase method produces highly pure, conductive FLG, while the in-flight gas-phase mixing strategy demonstrated here offers intrinsic advantages over conventional wet-chemical routes.

The use of harmful chemicals such as nitric acid, sulfuric acid, permanganate, chlorate, and hydrazine, which are used in the production of GO[71] and its conversion to reduced graphene oxide (rGO),[72,73] as well as the challenges of their disposal, are completely avoided with gas phase synthesis. The main by-products are ethylene, acetylene, CO, and hydrogen,[42] which can be reused in a closed manufacturing process. While a comprehensive evaluation of the environmental footprint, including techno-economic and life-cycle considerations, can be a natural next step, these characteristics suggest that the environmental footprint of the approach may be favorably impacted by reduced process complexity and waste generation. Collectively, the combination of high-purity FLG, low percolation thresholds, and single-step gas-phase assembly positions the Si–FLG heterostructures as a scalable and materials-efficient platform for high-capacity, stable Li-ion anodes, while establishing a generalizable framework that can be extended to other energy-efficient gas-phase synthesis routes.

3. Conclusions

This study establishes a one-step gas-phase strategy for the direct integration of silicon nanoparticles with FLG, enabling precise control over composition, structure, and electrochemical function. By adjusting precursor flow rates, we obtained heterostructures in which amorphous Si nanoparticles are uniformly anchored onto conductive FLG sheets. Structural analyses confirmed that FLG retained its integrity throughout the process, while enhancing surface area and establishing continuous electronic pathways in the heterostructures. Electrochemical testing revealed that the Si-FLG heterostructures significantly outperform pristine Si and slurry-mixed controls, with the optimized composition (15 wt% FLG) delivering superior performance alongside reduced impedance growth and preserved lithiation/delithiation features. These improvements are attributed to the dual role of FLG in enhancing conductivity and buffering Si volume expansion, thereby maintaining both structural integrity and long-term reversibility. Beyond benchmarking electrochemical gains (see Table S3, Supporting Information), the work highlights the broader significance of gas-phase synthesis as a scalable and versatile platform for engineering heterostructures. Unlike liquid-phase routes, direct gas-phase mixing enables the in-situ assembly of highly pure FLG with nanoparticles, unlocking the intrinsic potential of FLG as both a conductive scaffold and a mechanical stabilizer. Such an approach not only advances the design of Si/carbon anodes for high-performance Li-ion batteries but also opens new opportunities for tailoring gas-phase-synthesized FLG into multifunctional heterostructures across next-generation energy storage technologies.

4. Experimental Details

Synthesis of FLG: Two gas-phase reactors were integrated to enable in-flight mixing of their effluents: a MW plasma reactor producing FLGs and a hot-wall reactor producing nano silicon (nSi). The MW-assisted plasma synthesis was previously reported by Dato et al.[41] The plasma is initiated inside a quartz tube with an inner diameter of 70 mm, positioned within a cylindrical slot antenna (Cyrannus, iplas GmbH). MWs were produced with a Muegge magnetron head (Muegge GmbH MH 20005-213BA) at a maximum power of 2 kW and a drive frequency of 2.45 GHz.

The process begins with reactor evacuation to $\sim 2 \times 10^3$ Pa followed by the introduction of Ar, which acts as a sheath/plasma gas. The plasma is ignited at a MW power of 600 W. Hydrogen (H_2) gas is introduced to stabilize the Ar plasma at higher pressures and to avoid arcing. The plasma gases are introduced into the reactor through a fluid-dynamically optimized nozzle system, ensuring a stable vortex flow. The pressure and MW power gradually increased up to 10^5 Pa and 1400 W. The carbon-based precursor (ethanol/C_2H_5OH) is mixed with Ar and vaporized with the help of a controlled evaporation mixer (CEM W-209-333-P, Bronkhorst) and axially supplied into the reactor. To ensure stable plasma behavior, calibrated Bronkhorst mass flow controllers were used to precisely regulate the flow rates, typically maintaining 30 slm for Ar, 1 slm H_2, and 0.5 mL min^{-1} for C_2H_5OH. Throughout the process, the reactor remains at constant pressure, supported by a feedback-controlled venting system to offer stability and uniform precursor decomposition. Finally, FLG flakes are carried by the gas stream towards the filter. Our recently published work (Ref. [43]) shows that the precursor ethanol decomposes due to the high temperatures in the plasma (about 3500 K), releasing carbon that nucleates during the reaction. Following nucleation, single-layer graphene flakes with a diameter of several hundred nanometers initially form, which then fold into an average of about 6–8 layers of graphene as growth continues, as confirmed by the determination of the SSA. Graphene produced using this bottom-up approach is commonly referred to in the literature as FLG or GPG and differs structurally from GO, which is synthesized by oxidation of graphite and subsequent exfoliation. The reduction of GO via chemical or thermal processes leads to rGO.

Synthesis of silicon nanoparticles: In parallel, nSi are synthesized in a hot wall reactor, where monosilane (SiH_4) is pyrolyzed under precisely regulated conditions to create nSi. The details of the Si synthesis method can be found in previous publications from our research group.[39,40] Ar diluted SiH_4 (10% SiH_4 in Ar, quality: Air Liquide, extra high purity) is used as a precursor. In addition, Ar is also injected into the reactor through a separate inlet as a sheath gas and to prevent newly formed nanoparticles from depositing on the reactor wall.

Typically, a 10% SiH_4 mixture was directed into the hot-wall reactor, which featured a Degussit Al_2O_3 ceramic tube with an inner diameter of 60 mm and a 1 m heating jacket (SAF Wärmetechnik GmbH) powered by a 2.5 kW heating system, to pyrolyze SiH_4 into Si and H_2 at a temperature of 800 °C. Different flow rates for precursor gas mixture and sheath gas were used to introduce different Si concentrations in the heterostructures. The overall flow rate of gases in the reactor was fixed at 5 slm as shown in Table 1. As the gas mixture flows through the reactor, the high temperature breaks down SiH_4 into Si and H_2, which triggers the homogeneous nucleation of Si with subsequent nanoparticle growth to form nSi.

Synthesis of Si-FLG heterostructures: The outlets of both plasma and hot-wall reactors were connected at a precisely optimized junction, and their gas streams are merged to form a single flow directed toward a downstream filter. The schematic diagram of the combined reactor system is shown in **Figure 7**. Throughout the entire synthesis process, the reactor system was maintained at uniform pressure regulated by a common venting unit. Upon establishing a stable plasma under the desired synthesis conditions, both precursors were introduced simultaneously into the reactors. This configuration enables the synthesis of Si–FLG heterostructures with production rates of 700–1000 mg h^{-1}, depending on the precursor flow rate. The resulting heterostructures were continuously collected on a polytetrafluoroethylene membrane filter. To achieve heterostructures with varied Si content, different flow rates of Si precursor were used, as shown in **Table 1**. Additionally, individual components (nSi and FLG) were also obtained with consistent experimental conditions as benchmark materials. In this manuscript, from this point onwards, Si–FLG heterostructures are denoted SXXX, where XXX codes index the nominal SiH_4 flow rate in the hot-wall reactor; larger values correspond to higher SiH_4 flow. The four compositions studied are S150 (30 wt.% FLG), S300 (15 wt.% FLG), S450 (5 wt.% FLG), and S600 (8 wt.% FLG). Unless otherwise stated, "% FLG" refers to wt.% derived from combustion C analysis and corroborated by TGA and DSC.

Materials characterization: Simultaneous thermal analysis (STA), incorporating both TGA and DSC, was performed using a Netzsch STA 449 F1 Jupiter (Germany). The measurements were conducted under a synthetic air atmosphere with a heating rate of 10 K min^{-1} up to 1200 °C, and released gaseous species were analyzed simultaneously with a quadrupole mass spectrometer. In addition to STA, bulk carbon content was determined by combustion elemental analysis (Leco, CS744). The powder-averaged total carbon was used to quantify the graphene mass fraction in the Si–FLG heterostructures.

TEM (JEOL, JEM-2200FS) was used for morphological analysis of the heterostructures. SSAs were measured via N_2 physisorption conducted on a Quantachrome Nova 2200 instrument, based on the BET method. The morphological

Table 1. Different flow rates through the hot wall reactor to produce Si nanoparticles, FLG, and Si–FLG heterostructures with different concentrations of Si.

Sample name	Precursor gas mixture (10% SiH_4 in Ar)	Sheath gas (Ar)	Overall gas flow
FLG[a]	0 mL min^{-1}**	5 slm***	5 slm
nSi	300 mL min^{-1}	4.85 slm	5 slm
S150	150 mL min^{-1}	4.85 slm	5 slm
S300	300 mL min^{-1}	4.70 slm	5 slm
S450	450 mL min^{-1}	4.55 slm	5 slm
S600	600 mL min^{-1}	4.40 slm	5 slm

[a]Few-layer graphene
**mL min^{-1} (mili liters per minute)
***slm (standard liters per minute)

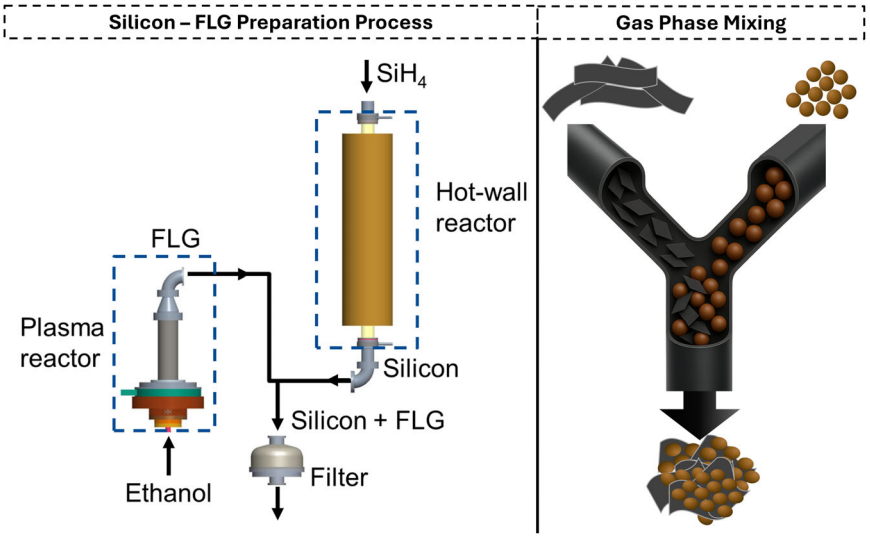

Figure 7. Schematic diagram for an integrated reactor system involving a microwave (MW) plasma reactor for the synthesis of graphene and a hot wall reactor production of silicon nanoparticles.

analysis of the cast electrodes of Si–FLG heterostructures was examined by SEM (Hitachi SU8700) at an acceleration voltage of 3 kV.

Micro Raman spectroscopy (Renishaw inVia) was performed to analyze the crystallinity of nSi and the carbon allotropes. The device was operated with a 633 nm Nd:YAG laser and a diffraction grating of 1800 lines mm^{-1}. XRD measurements were acquired through a Bruker D8 Advance diffractometer using Cu K_α radiation. Four-point probe measurements were performed with the help of a Karl Suss PM5 probe station to evaluate the electronic conductivity. A constant current was applied using a Keithley 2400 source meter, while the voltage was measured with a Keithley 2700 multimeter.

Electrode and cell fabrication: Si-FLG heterostructures were processed to evaluate their performance as anode materials in Li-ion batteries. The processing strategy followed for this study is reported for nSi and its composites in the literature.[7] Slurries of the active material were prepared and cast onto copper (Cu) current collectors using a doctor blade. The wet thickness of the casting was set at 50 µm, and the mass loading was maintained to ~0.5–1 mg cm^{-2}. After casting, the electrodes were dried in a vacuum oven at a temperature of 80 °C for 12 h. The dried electrodes comprised 75 wt.% active material, 10 wt.% conductive carbon (Super C65), and 15 wt.% binder (polyacrylic acid). 2032-type coin cells were assembled in an Ar-filled glove box with the Si-FLG anode as the working electrode, a Li metal disc as the reference electrode, a 1 M solution of $LiPF_6$ in EC: DMC (50:50 by weight) as the electrolyte, and a Whatman GF/D glass fiber separator.

Electrochemical characterization: Electrochemical galvanostatic cycling was carried out at 25 °C in the voltage range of 0.01–1.2 V. Formation cycle was conducted at 0.05C and long-term cycling was conducted at 1C for 100 cycles. All the long-term cycling tests were conducted using an electrochemical workstation (MACCOR battery tester). Furthermore, potentiostatic electrochemical impedance spectroscopy (EIS) tests were performed using a multichannel potentiostat (Biologic) over a frequency range of 1 MHz to 10 mHz.

Acknowledgements

The authors acknowledge financial support by the Deutsche Forschungsgemeinschaft (DFG; German Research Foundation, Germany) [IRTG 2803–461605777] and Natural Sciences and Engineering Research Council of Canada (NSERC) [CREATE 565360 and Discovery Grant RGPIN-2023-03932]. We thank Claudia Lopez Camara, Sabrina Schleich, and Beate Endres for TEM and BET measurements. The X-ray data were generated by the X-ray diffractometer from AG Schulz (Inorganic Chemistry, UDE). We thank Georg Bendt and Mohammed-Ali Sheikh for the assistance in using this instrument. We also acknowledge the Ontario Battery and Electrochemistry Research Centre (OBEC) for providing electrochemical testing facilities. Open Access funding enabled and organized by Projekt DEAL.

Conflict of Interest

The authors declare no conflict of interest.

Declaration of Generative AI and AI-Assisted Technologies

During the preparation of this work, the authors used the AI-assisted tool ChatGPT for English language editing and grammatical corrections. After using this service, the authors reviewed and edited the content as needed and take full responsibility for the content of the published article.

Data Availability Statement

Data is available on Zenodo, DOI: 10.5281/zenodo.18119350.

Supporting Information

Supporting Information is available from the Wiley Online Library or from the author.

Keywords

few-layer graphene, gas-phase synthesis, lithium-ion battery, microwave plasma synthesis, silicon nanoparticles

Received: November 25, 2025
Revised: January 16, 2026
Published online: February 4, 2026

[1] J. Liu, *Graphene-Based Composites for Electrochemical Energy Storage*, Springer Singapore, Singapore **2017**.
[2] M. F. El-Kady, Y. Shao, R. B. Kaner, *Nat. Rev. Mater.* **2016**, *1*, 16033.
[3] J. Liu, *Nat. Nanotechnol.* **2014**, *9*, 739.
[4] C. S. Bongu, S. Tasleem, M. R. Krishnan, E. H. Alsharaeh, *Sustain. Energy Fuels* **2024**, *8*, 4039.
[5] P. Sehrawat, A. Shabir, Abid, C. M. Julien, S. S. Islam, *J. Power Sources* **2021**, *501*, 45601.
[6] M. A. Rahman, G. Song, A. I. Bhatt, Y. C. Wong, C. Wen, *Adv. Funct. Mater.* **2016**, *26*, 647.
[7] A. Münzer, L. Xiao, Y. H. Sehlleier, C. Schulz, H. Wiggers, *Electrochim. Acta* **2018**, *272*, 52.
[8] B. Liang, Y. Liu, Y. Xu, *J. Power Sources* **2014**, *267*, 469.
[9] X. L. Wu, Y. G. Guo, L. J. Wan, *Chem. Asian J.* **2013**, *8*, 1948.
[10] W.-J. Zhang, *J. Power Sources* **2011**, *196*, 877.
[11] J. B. Kim, J. Baek, B. Jayaraman, S. Cha, G. S. Lee, Y. H. Yoon, G. B. Choi, C. W.-L. Cheng, J. Lim, H.-T. Kim, S. O. Kim, *ACS Energy Lett.* **2025**, *10*, 2718.
[12] J. Zhu, D. Yang, Z. Yin, Q. Yan, H. Zhang, *Small* **2014**, *10*, 3480.

[13] Y. Shang, H. Li, T. Ma, Y. Yang, Y. Jiang, W. Yu, *ACS Appl. Mater. Interfaces* **2025**, *17*, 31730.
[14] J. Reslan, M. Saadaoui, T. Djenizian, *Adv. Mater. Interfaces* **2024**, *11*, 2301062.
[15] M. Ko, S. Chae, J. Cho, *ChemElectroChem* **2015**, *2*, 1645.
[16] J. K. Lee, K. B. Smith, C. M. Hayner, H. H. Kung, *Chem. Commun.* **2010**, *46*, 2025.
[17] X. Zhao, C. M. Hayner, M. C. Kung, H. H. Kung, *Adv. Energy Mater.* **2011**, *1*, 1079.
[18] H. Xiang, K. Zhang, G. Ji, J. Y. Lee, C. Zou, X. Chen, J. Wu, *Carbon (N. Y.)* **2011**, *49*, 1787.
[19] B. P. N. Nguyen, N. A. Kumar, J. Gaubicher, F. Duclairoir, T. Brousse, O. Crosnier, L. Dubois, G. Bidan, D. Guyomard, B. Lestriez, *Adv. Energy Mater.* **2013**, *3*, 1351.
[20] W. J. Lee, T. H. Hwang, J. O. Hwang, H. W. Kim, J. Lim, H. Y. Jeong, J. Shim, T. H. Han, J. Y. Kim, J. W. Choi, S. O. Kim, *Energy Environ. Sci.* **2014**, *7*, 621.
[21] S. Yang, G. Li, Q. Zhu, Q. Pan, *J. Mater. Chem.* **2012**, *22*, 3420.
[22] D. Chen, R. Yi, S. Chen, T. Xu, M. L. Gordin, D. Wang, *Solid State Ionics* **2014**, *254*, 65.
[23] X. Xin, X. Zhou, F. Wang, X. Yao, X. Xu, Y. Zhu, Z. Liu, *J. Mater. Chem.* **2012**, *22*, 7724.
[24] S.-L. Chou, J.-Z. Wang, M. Choucair, H.-K. Liu, J. A. Stride, S.-X. Dou, *Electrochem. Commun.* **2010**, *12*, 303.
[25] L. Fei, B. P. Williams, S. H. Yoo, J. Kim, G. Shoorideh, Y. L. Joo, *ACS Appl. Mater. Interfaces* **2016**, *8*, 5243.
[26] Q. Pan, P. Zuo, S. Lou, T. Mu, C. Du, X. Cheng, Y. Ma, Y. Gao, G. Yin, *J. Alloys Compd.* **2017**, *723*, 434.
[27] M. Su, S. Liu, L. Tao, Y. Tang, A. Dou, J. Lv, Y. Liu, *J. Electroanal. Chem.* **2019**, *844*, 86.
[28] X. Hu, Y. Jin, B. Zhu, Z. Liu, D. Xu, Y. Guan, M. Sun, F. Liu, *J. Colloid Interface Sci.* **2018**, *532*, 738.
[29] W. Zhai, Q. Ai, L. Chen, S. Wei, D. Li, L. Zhang, P. Si, J. Feng, L. Ci, *Nano Res.* **2017**, *10*, 4274.
[30] J. Yang, J. Liu, C. Zhao, W. Zhang, X. Li, *Mater. Lett.* **2020**, *266*, 127484.
[31] M. H. Lin, S. Hy, C. Y. Chen, J. H. Cheng, J. Rick, N. W. Pu, W. N. Su, Y. C. Lee, B. J. Hwang, *ChemElectroChem* **2016**, *3*, 1446.
[32] X. Li, X. Tian, N. Zhao, K. Wang, Y. Song, Q. Guo, C. Chen, L. Liu, *New J. Chem.* **2016**, *40*, 8961.
[33] J. Lin, J. He, Y. Chen, Q. Li, B. Yu, C. Xu, W. Zhang, *Electrochim. Acta* **2016**, *215*, 667.
[34] J. B. Kim, S. H. Koo, I. H. Kim, J. T. Kim, J. G. Kim, B. Jayaraman, J. Lim, S. O. Kim, *Chem. Eng. J.* **2022**, *446*, 137390.
[35] M. T.-U. Safian, K. Umar, M. N. Mohamad Ibrahim, *J. Clean. Prod.* **2021**, *318*, 128603.
[36] I. Levchenko, K. Ostrikov, J. Zheng, X. Li, M. Keidar, K. B. K. Teo, *Nanoscale* **2016**, *8*, 10511.
[37] P. Fortugno, C.-F. López-Cámara, J. P. Kruse, M. Hammad, H. Wiggers, *Adv. Eng. Mater.* **2023**, *25*, 2300679.
[38] M. Hammad, S. Angel, A. K. Al-Kamal, A. Asghar, A. Said Amin, M.-A. Kräenbring, H. T. A. Wiedemann, V. Vinayakumar, M. Yusuf Ali, P. Fortugno, C. Kim, T. C. Schmidt, C. W. M. Kay, C. Schulz, D. Segets, H. Wiggers, *Chem. Eng. J.* **2023**, *454*, 139900.
[39] M. Loewenich, H. Orthner, P. Wollny, I. Wlokas, S. Bade, J. Lyubina, H. Wiggers, *J. Alloys Compd.* **2024**, *986*, 174061.
[40] H. Orthner, H. Wiggers, M. Loewenich, S. Kilian, S. Bade, J. Lyubina, *J. Alloys Compd.* **2021**, *870*, 159315.
[41] A. Dato, V. Radmilovic, Z. Lee, J. Phillips, M. Frenklach, *Nano Lett.* **2008**, *8*, 2012.
[42] P. Fortugno, S. Musikhin, X. Shi, H. Wang, H. Wiggers, C. Schulz, *Carbon* **2022**, *186*, 560.
[43] C.-F. López-Cámara, P. Fortugno, M. Heidelmann, H. Wiggers, C. Schulz, *Carbon* **2024**, *218*, 118732.
[44] S. Lin, X. Li, J. Zhang, L. Guo, X. Xu, W. Yuan, H. Liu, A. Li, X. Chen, H. Song, *J. Colloid Interface Sci.* **2025**, *699*, 138302.
[45] A. Y. Kharin, Y. V. Kargina, V. Y. Timoshenko, *J. Nanopart. Res.* **2019**, *21*, 27.
[46] F. Farivar, P. Lay Yap, R. U. Karunagaran, D. Losic, *C.* **2021**, *7*, 41.
[47] A. G. Bannov, M. V. Popov, P. B. Kurmashov, *J. Therm. Anal. Calorim.* **2020**, *142*, 349.
[48] Y. J. Chabal, *Fundamental Aspects of Silicon Oxidation*, 1st ed., Springer Berlin Heidelberg, Berlin, Heidelberg **2001**.
[49] M. Vazquez-Pufleau, *SILICON* **2021**, *13*, 189.
[50] F. Xu, G. Nava, P. Biswas, I. Dulalia, H. Wang, Z. Alibay, M. Gale, D. J. Kline, B. Wagner, L. Mangolini, M. R. Zachariah, *Chem. Eng. J.* **2022**, *430*, 133140.
[51] M. C. Heine, S. E. Pratsinis, *Langmuir* **2007**, *23*, 9882.
[52] N. A. Fuks, C. N. Davies, *The Mechanics of Aerosols* Revised and Enlarged Edition, Dover Publications, New York, NY **1989**.
[53] C.-F. López-Cámara, P. Fortugno, M. Asif, S. Musikhin, C. Prindler, H. Wiggers, T. Endres, N. Eaves, K. J. Daun, C. Schulz, *Combust. Flame* **2023**, *258*, 112713.
[54] D. M. Zhigunov, G. N. Kamaev, P. K. Kashkarov, V. A. Volodin, *Appl. Phys. Lett.* **2018**, *113*, 23101.
[55] A. K. Verma, J. Singh, P. Nguyen-Tri, *ACS Appl. Mater. Interfaces* **2024**, *16*, 10969.
[56] J.-B. Wu, M.-L. Lin, X. Cong, H.-N. Liu, P.-H. Tan, *Chem. Soc. Rev.* **2018**, *47*, 1822.
[57] Y. Hwangbo, C.-K. Lee, A. E. Mag-Isa, J.-W. Jang, H.-J. Lee, S.-B. Lee, S.-S. Kim, J.-H. Kim, *Carbon* **2014**, *77*, 454.
[58] L. G. Cançado, K. Takai, T. Enoki, M. Endo, Y. A. Kim, H. Mizusaki, A. Jorio, L. N. Coelho, R. Magalhães-Paniago, M. A. Pimenta, *Appl. Phys. Lett.* **2006**, *88*, 163106.
[59] L. Wang, P. Makk, S. Zihlmann, A. Baumgartner, D. I. Indolese, K. Watanabe, T. Taniguchi, C. Schönenberger, *Phys. Rev. Lett.* **2020**, *124*, 157701.
[60] I. Miccoli, F. Edler, H. Pfnür, C. Tegenkamp, *J. Phys. Condens. Matter* **2015**, *27*, 223201.
[61] T. Kaiser, G. Dehm, C. Kirchlechner, A. Menzel, H. Bishara, *Eur. J. Mech.* **2023**, *97*, 104777.
[62] H. Minagawa, S. Miyamoto, I. Kurashige, M. Hisada, *Constr. Build. Mater.* **2023**, *374*, 130784.
[63] Y. Wang, S. Lu, W. He, S. Gong, Y. Zhang, X. Zhao, Y. Fu, Z. Zhu, *Sci. Rep.* **2022**, *12*, 10448.
[64] L. Sun, J. Wang, E. Bonaccurso, *Sci. Rep.* **2013**, *3*, 1991.
[65] J. Lee, G. Oh, H.-Y. Jung, J.-Y. Hwang, *Inorganics* **2023**, *11*, 182.
[66] N. Xu, L. Jiang, H. Zhou, H. Chu, P. Jiang, *J. Wuhan Univ. Technol. Mater. Sci. Ed.* **2021**, *36*, 804.
[67] R. Maddipatla, C. Loka, K.-S. Lee, *ACS Appl. Mater. Interfaces* **2023**, *15*, 58437.
[68] H. Li, Y. Lai, H. Li, Q. Yang, Z. Yang, Z. Zheng, Y. Liu, Y. Sun, B. Zhong, Z. Wu, X. Guo, *Ind. Eng. Chem. Res.* **2022**, *61*, 13431.
[69] Q. Huang, M. J. Loveridge, R. Genieser, M. J. Lain, R. Bhagat, *Sci. Rep.* **2018**, *8*, 1386.
[70] M. J. Loveridge, M. J. Lain, Q. Huang, C. Wan, A. J. Roberts, G. S. Pappas, R. Bhagat, *Phys. Chem. Chem. Phys.* **2016**, *18*, 30677.
[71] W. S. Hummers, R. E. Offeman, *J. Am. Chem. Soc.* **1958**, *80*, 1339.
[72] X. Li, L. Zhi, *Chem. Soc. Rev.* **2018**, *47*, 3189.
[73] S. Park, R. S. Ruoff, *Nat. Nanotechnol.* **2009**, *4*, 217.